Development of an APD-Based PET Module and Preliminary Resolution Performance of an Experimental Prototype Gantry

Jun Kataoka, Hidenori Matsuda, Fumihiko Nishikido, Makoto Koizumi, Hirokazu Ikeda, Masao Yoshino, Takamasa Miura, Satoshi Tanaka, Yoshitaka Ishikawa, Nobuyuki Kawabata, Keiji Shimizu, Yusuke Matsunaga, Shunji Kishimoto, Hidetoshi Kubo, Yoshio Yanagida, and Takeshi Nakamori

***Abstract*—The development of a high-resolution Positron Emission Tomography (PET) technique with sub-millimeter spatial resolution, which utilizes newly designed reverse-type APD-arrays, is uderway. All the detector blocks are modularized with the overall dimension of each module, including the APD array, LYSO scintillator matrix and Front-End Circuits (FECs), which are only $30 \times 30 \times 80\ \mathrm{mm}^3$. Each APD device also has a monolithic 16×16 pixel structure with an active area of $1.0\ \mathrm{mm}^2$ per pixel. The FEC includes two identical analog ASICs specifically designed for APDs with a noise characteristic of $560 + 30\ \mathrm{e}^-/\mathrm{pF}$ and a timing resolution of 460 ps (rms), respectively. An energy resolution of 13.7 $\pm$ 1.1% (FWHM) with 662 keV gamma-rays was measured using the 16×16 arrays. At this stage a pair of module and coincidence circuits has been assembled into an experimental prototype gantry. Spatial resolutions of 0.9, 1.4, and 1.3 mm (FWHM) were obtained from FBP reconstructed images in preliminary experiments with a point source positioned centrally, and 1 and 5 mm off-center, respectively. Comparison with a Monte-Carlo simulation of a fully-designed gantry over a wider range of field-of-view showed good correlation with the experimental data. A simple but conceptual design of a DOI configuration is also proposed as a test example of a future APD-PET scanner.**

***Index Terms*—Avalanche photodiode, Depth-Of-Interaction (DOI), image reconstruction, Positron Emission Tomography (PET).**

Manuscript received March 02, 2010; revised June 03, 2010; accepted June 25, 2010. Date of publication August 30, 2010; date of current version October 15, 2010.

J. Kataoka, H. Matsuda, M. Yoshino, T. Miura, and T. Nakamori are with the Research Institute for Science and Engineering, Waseda University, Shinjuku, Tokyo 169-85555, Japan (e-mail: kataoka.jun@waseda.jp; aken.matsu@gmail.com; ymasa1241@gmail.com; miura-tkms.eijo@toki.waseda.jp; nakamori@aoni.waseda.jp).

F. Nishikido is with the National Institute of Radiological Sciences, Inage-ku, Chiba 263-8555, Japan (e-mail: funis@nirs.go.jp).

M. Koizumi and S. Tanaka are with the Tokyo Institute of Technology, Meguro-ku, Tokyo 152-8550, Japan (e-mail: koizumi@hp.phys.titech.ac.jp; stanaka@hp.phys.titech.ac.jp).

H. Ikeda is with ISAS/JAXA, Sagamihara, Kanagawa 229-8510, Japan (e-mail: ikeda.hirokazu@jaxa.jp).

Y. Ishikawa, N. Kawabata, K. Shimizu, and Y. Matsunaga are with Hamamatsu Photonics, K.K., Naka-ku, Hamamatsu City, Shizuoka Pref. 430-8587, Japan (e-mail: yoshi-i@ssd.hpk.co.jp; kawabata@hq.hpk.co.jp; keiji@crl.hpk.co.jp; yu-matsu@ssd.hpk.co.jp).

S. Kishimoto is with KEK-PF, Tsukuba, Ibaraki 305-0801, Japan (e-mail: syunji.kishimoto@kek.jp).

H. Kubo is with Kyoto University, Kyoto 606-8502, Japan (e-mail: kubo@cr.scphys.kyoto-u.ac.jp).

Y. Yanagida is with WES, Kyoto 607-8188, Japan (e-mail: yanagidayoshio@nifty.com).

Color versions of one or more of the figures in this paper are available online at http://ieeexplore.ieee.org.

Digital Object Identifier 10.1109/TNS.2010.2055889

I. Introduction

THE recent onset of the use of dual modality PET/CT imaging has had a profound effect on clinical diagnoses made in radiology, oncology and other areas of nuclear medicine. However, CT imaging suffers from poor soft-tissue contrast, with patients also subjected to a significant radiation dose that exceeds that received from the PET itself. In contrast, Magnetic Resonance Imaging (MRI) offers excellent soft-tissue contrast and anatomical detail without the additional radiation. Unfortunately, the Photo-Multiplier Tube (PMT) incorporated in a PET scanner is difficult to use within the MRI high magnetic field. Moreover, the spatial resolution attainable with a PMT-based PET (typically >5 mm with a whole body PET and >2 mm with an animal PET) is far from the theoretical limit of the PET resolution ($\leq$ 1 mm). An APD [1] is a compact high performance light-sensor that could also be used in the MRI (e.g., [2], [3]). Moreover, given the advantage of pixel miniaturization, the application of such APD can be anticipated in dense position sensitive detectors. Currently APD-based PET modules have been proposed or tested in small animal PET scanners, while novel high resolution PET scanners using APDs and LYSO/LGSO have also been proposed (e.g., LabPET: [4], MADPET-II: [5]). Also, RatCap is the first portable brain scanner for awake rats [6]–[9], which successfully demonstrated the potential for (1) an intrinsic spatial resolution as good as 2.1 mm and (2) preliminary simultaneous PET/MRI imaging. A similar high-resolution small animal PET scanner with silicon pad detectors [10] as well as Geiger-mode APDs [11] are also being proposed but remain in a far earlier developmental phase than the RatCap. The integration and end-to-end test of a newly developed APD-based PET module capable of achieving the ultimate sub-millimeter spatial resolution will be described here. Although the application in a small-animal PET device was assumed in the preliminary performance verification tests, the module remains very compact and easily extendable for use in brain PET and whole body PET scanners. Moreover, multi-channel (32ch) ASICs with timing capabilities are being developed to read the fast APD signals, and for future application in a Time-Of-Flight (TOF) capable PET scanner.

II. Materials

A. APD-Array

Three types of large-area, reverse-type APD-arrays [12], [13] were designed and developed in cooperation with Hamamatsu

TABLE I
BASIC CHARACTERISTICS OF NEWLY DEVELOPED APD-ARRAYS

	TYP-I	TYP-II
Matrix Array	8x8	16x16
Pixel Size [mm]	2x2	1x1
I_D (M=50) [nA]	0.5-1.3	0.1-0.3
V_{brk} [V]	379	376
V_R (M=50) [V]	355	333
Capacitance [pF]	13-15	4-5

I_D = dark current, V_{brk} = break down voltage; V_R = operation bias to achieve APD gain of $M = 50$.

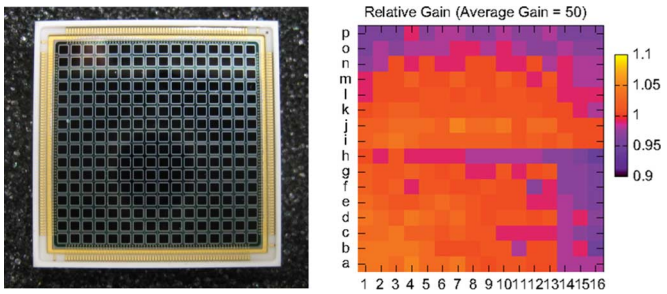

Fig. 1. (left) A picture of the APD-array TYP-II. (right) Gain uniformity of the APD-array TYP-II operated at a gain $M = 50$.

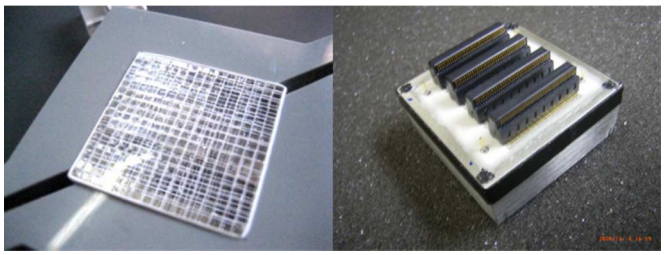

Fig. 2. (left) A picture of LYSO scintillator matrix (16 × 16 pixel arrays of $1.3 \times 1.3 \times 10$ mm^3 each) and (right) sensor head coupled with APD-array TYP-II.

Photonics K.K. Table I lists the design parameters, and the dark noise and gain characteristic of the APD device tested in this paper [14]. All the APD-arrays are embedded in a ceramic package of the same configuration and 27.4×27.4 mm^2 in size. Below the TYP-II APD-array (a 16 × 16 pixel structure with an active area of 1.0×1.0 mm^2 per pixel and a 0.4 mm gap between the pixels) in particular was used in the test fabrication of an APD-based PET module. Fig. 1 provides a photo of a TYP-II APD-array (left) and the gain uniformity (right) obtained at $M = 50$. Note that the gain variation is less than 10% of the 256 pixels. The APD-array supported stable operation at a gain of up to 100 with extremely low dark noise (less than 1 nA) for each pixel, even at room temperature. An avalanche gain of 50 was achieved with a bias voltage of 330–360 V, which is sufficiently lower than with usual PMTs (∼1000 V).

B. LYSO Scintillator Matrix

A prototype gamma-ray camera consisting of an APD array optically coupled to a LYSO matrix was fabricated in World Engineering System (WES) in Japan. The ratio of Lu in the crystal is close to 71%. Fig. 2 (left) provides a photo of the 16 × 16 LYSO matrix used in the TYP-II APD, with each pixel $1.3 \times 1.3 \times 10$ mm^3 in size and with a polished surface, divided by the lattice of a thin reflective layer (3M ESR). Fig. 2 (right) provides a photo of the TYP-II APD-array coupled with the LYSO matrix. Note that the output signals from the APDs are divided into four 70-pin connectors on the rear panel of the ceramic package and are hence directly connectable to the Front-End-Circuit (FEC), as described below.

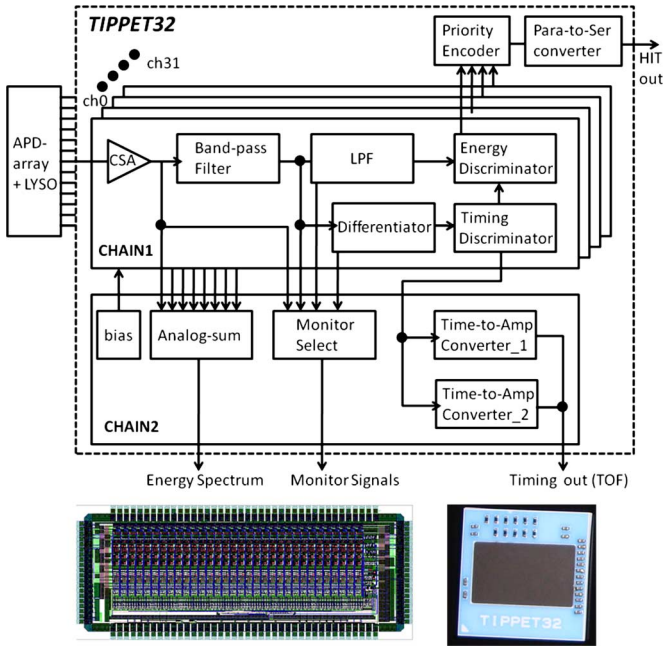

Fig. 3. (upper) A circuit architecture of TIPPET32. (bottom left) A chip layout of TIPPET32. Tip size is 2.85 mm × 7.35 mm. (bottom right). LTCC package for TIPPET32. Package size is 13 mm × 13 mm.

C. Front-End ASIC

To read the APD signals with the moderate amplification gain of M ∼ 50–100 a high-speed, low-noise, 32-channel analog ASIC designated the "TIPPET32" was developed as an improved version of the 8-channel ASIC reported in [15]. The TIPPET32 chip was implemented using TSMC 0.35 μm CMOS technology and mounted in a Low Temperature Co-fired Ceramic (LTCC) package (Fig. 3: bottom right). The LTCC chip is 13×13 mm^2 in size with a maximum power dissipation of 210 mW (6.6 mW/ch) for power rails of ±1.65 V. The design and architecture of the TIPPET32 chip is detailed below. Each ASIC includes 32-channel charge-sensitive amplifiers, band-pass filters, differentiators, pulse-height and timing discriminators, and two-channel time-to-amplitude converters. The Equivalent Noise Charge (ENC) was measured at $560 + 30$ e$^-$/pF (rms). When actually used in the PET system each of the ASICs are implemented on a Front-End-Card (FEC) that is directly connectable to the rear end of the APD ceramic package (Fig. 2; right). The FEC includes two identical TIPPET32 chips, two ADCs, a DAC, a low-pass filter, and an 8-bit shift register. It is 30×60 mm^2 in size with a power

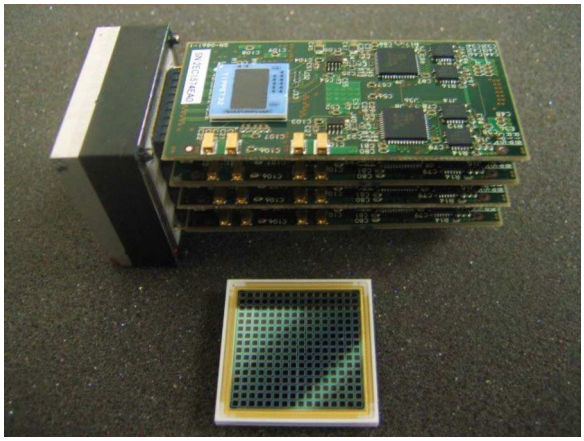

Fig. 4. An APD-based PET module consisting of large-area APD-array coupled with LYSO matrix, and analog FEC connected directly rear-end of the APD ceramic package.

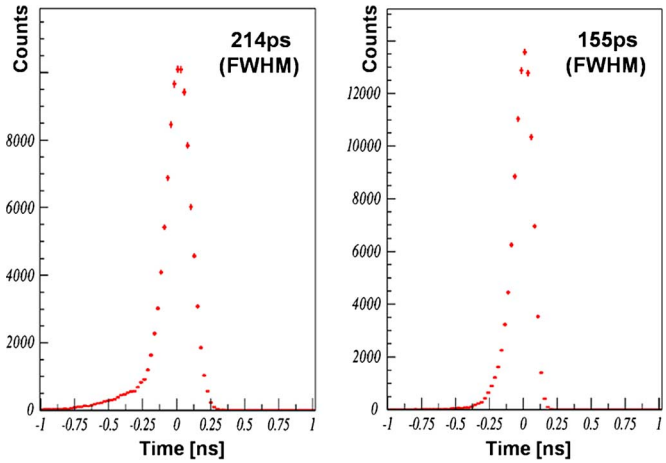

Fig. 5. Time resolutions for APD-arrays TYP-I (left) and TYP-II (right), measured at KEK-PF, with 10 keV synchrotron monochromatic X-ray beam.

consumption of 0.9 W/board (refer also to Fig. 4 for the FEC geometry).

D. Fabrication of the APD-Based PET Module

Combining all the detector components resulted in the versatile APD-based PET module shown in Fig. 4. The module consists of a gamma-ray sensor head (large area APD-array with one to one coupling to a LYSO crystal array) and four FECs connected to the rear-end of the APD package. The module is only $30 \times 30 \times 80\ \mathrm{mm}^3$ in size, which is extremely compact when compared to the typical size of PMT-based PET scanners.

III. Methods

A. Timing Response of the APD-Array

A timing experiment involving the APD-arrays was carried out at beam line 14A of the PF ring (KEK) in Tsukuba, Japan. A double-crystal silicon (111) monochromator was used to define the X-ray energy of 10 keV (in mimicking the output charge of 511 keV gamma-rays on LYSO scintillators). During the experiment, the beam at KEK-PF was operated in single-bunch mode. The figures below reveal the time response of the APD-arrays operated at an avalanche gain of 100. The measured time resolution provided $\Delta \mathrm{T} = 214\ \mathrm{ps}$ with the 8×8 TYP-I array and 155 ps (FWHM) with the TYP-II 16×16 APD arrays, respectively (Fig. 5).

B. ASIC Performance

The energy resolution of the analog front-end was measured using a $^{22}\mathrm{Na}$ source and a $2 \times 2 \times 10\ \mathrm{mm}^3$ LYSO pixel scintillator coupled to a single $2 \times 2\ \mathrm{mm}^2$ APD pixel device implemented in a $10.6 \times 9.0\ \mathrm{mm}^2$ ceramic package. The surface area and internal structure of this APD device is completely the same as those used in a TYP-I APD-array. The surface of the LYSO pixel is polished, and Teflon tape was used as a reflector. Excellent energy resolutions of 11.8% (FWHM) and 10.0% (FWHM) were obtained respectively, at 511 and 662 keV (Fig. 6 (left)). The noise threshold was set at 50 keV. The electronic timing resolution of the analog front-end was then measured using a test pulser and calibrated with an external TAC module (ORTEC 566). The input pulse amplitude was set at a photo peak level of 511 keV in the experiment. A timing resolution of 460 ps (rms) was obtained for the ASIC alone, being slightly worse (550 ps rms) when coupled with an APD as revealed in Fig. 6 (right).

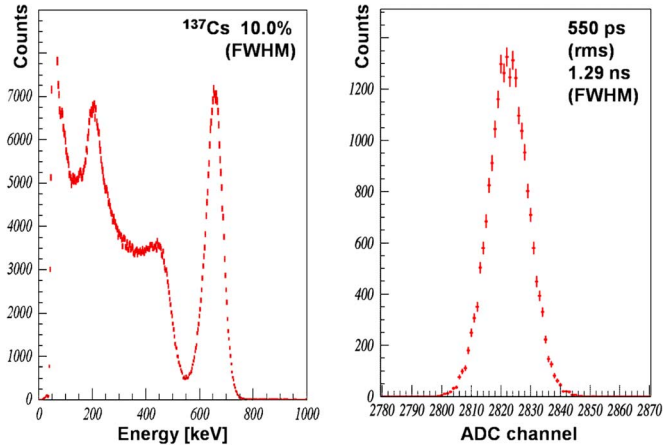

Fig. 6. (left) Energy spectrum for 662 keV gamma-rays, and (right) time resolution of analog ASIC measured with a small LYSO pixel scintillator coupled with an $2 \times 2\ \mathrm{mm}^2$ APD pixel.

C. Test of the Integrated Module

The initial performance of an integrated APD-based PET module (see, Fig. 4) including an APD-array, LYSO matrix, and analog front-end, was tested by taking the energy spectrum of a $^{137}\mathrm{Cs}$ source of all the pixels (either 8×8 or 16×16 pixels). The average energy resolution of the 662 keV gamma-rays was $11.7 \pm 0.7\%$ (with TYP-I 8×8 array; FWHM) and $13.7 \pm 1.1\%$ (with TYP-II 16×16 array; FWHM), respectively. Fig. 7 (top) provides an example spectral matrix of 662 keV gamma-rays obtained with the TYP-II APD array and LYSO scintillators. Fig. 7 (bottom) shows the variation in signal amplitude and energy resolution measured with 662 keV gamma-rays (due to the inhomogeneity of the APD gain and LYSO light yield). Note that the variation of signal amplitude was less than $\pm 20\%$. The cross-talk of scintillation light from neighboring LYSO pixels was also measured at under 15%, which confirmed the ideal coupling of individual crystals to the

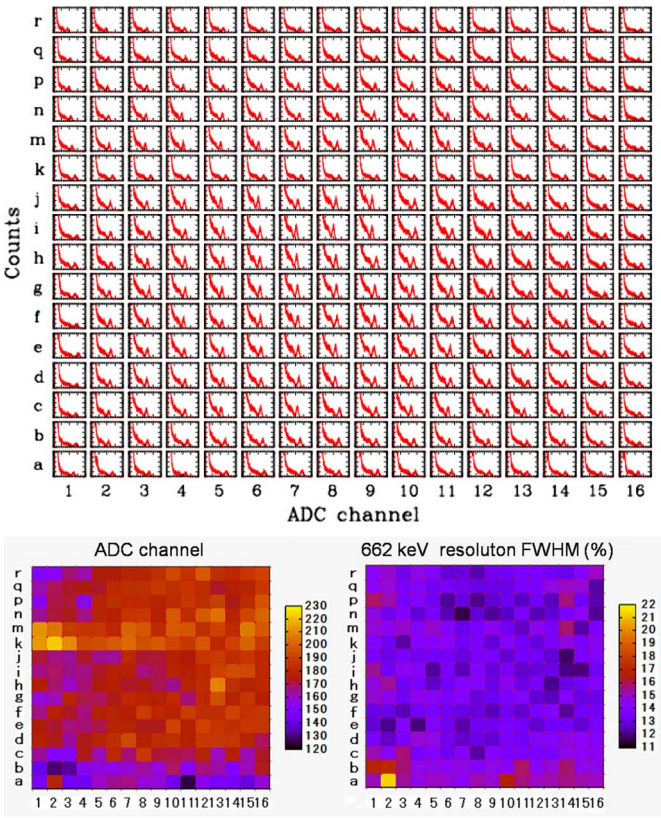

Fig. 7. (top) A distribution of pulse height spectra of 16 × 16 APD module (TYP-II APD plus LYSO matrix) irradiated by ^{137}Cs source. (bottom) Uniformity of pulse height (in the ADC channel) and energy resolution of 662 keV gamma-rays. The variation of signal pulse height was less than ±20% of the 256 pixels.

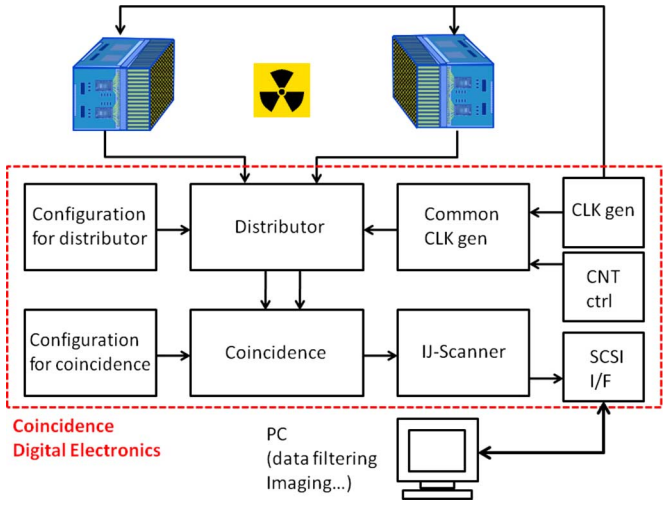

Fig. 8. System chart of imaging test experiments using two units of APD-based PET module developed in this paper.

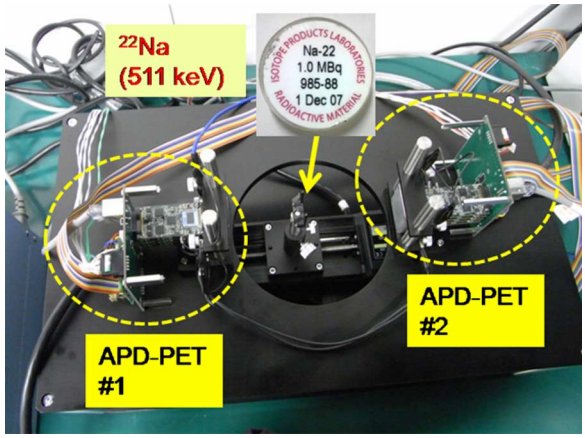

Fig. 9. Experimental setup of the prototype system for the point source measurements. Ring diameter of 150 mm ϕ.

APD pixels. This type of PET scanner (individual coupling) enables an intrinsic spatial resolution precisely equivalent to the geometric resolution; 0.8 mm (FWHM) with 16 × 16 array (1.4 mm for 8 × 8 array), and almost comparable to the theoretical limit determined for the noncollinearity and the positron range required for application in a PET scanner [7].

IV. Results and Discussions

A. The Prototype Gantry

A schematic diagram of the test system is provided in Fig. 8. The prototype system consists of a pair of APD-based PET detectors and a coincidence circuit. Output signals from the APD-based PET modules are fed into a digital circuit developed by Hamamatsu Photonics, K.K. If the timing signals from the APD-PET modules coincide within the time-window of 32 ns, the HIT address, timing, and valid flag are stored in a memory for use in creating list-mode data. All the data are sent to a DAQ system (Linux PC) connected via SCSI cable for further analysis, which includes noise filtering and imaging. A photo of the experimental setup is provided in Fig. 9. In a preliminary performance test, two APD-based PET detectors were set in place with an ^{22}Na isotope (1 MBq calibrated on 1 December, 2007, but 0.57 MBq at the measurement date) in-between. The plastic external frame of the source was 25 mm ϕ in diameter, but the ^{22}Na was doped within the central 0.25 mm ϕ region and could hence be regarded as a point source.

The position of the ^{22}Na isotope was then flexibly controlled using both the X-stage (SGSP 20-85, Sigma Koki) and the θ-stage (SGSP 80Y-AW, Sigma Koki) to evaluate the resolution performance, while the accuracy of the stage controllers was 1 μm/pulse and 2.5×10^{-3} deg/pulse, respectively.

B. Verification Test: Coincidence Matrix

As an initial step in subsequent imaging experiments >50,000 coincidence events were amassed and the correlation of fired channels between two facing APD-based PET modules investigated. The ^{22}Na point source was placed exactly in the center (x = 0 mm, θ = 0 deg). In Fig. 10 (left), the x-axis provides a sequence ID (from 1 to 16 in a tangential direction) of the fired APD pixels in module #1 and the y-axis that of module #2, as defined in the panel on the right. Only the events detected above the energy threshold of 250 keV are revealed in the diagram. Coincidence events originating from 511 keV

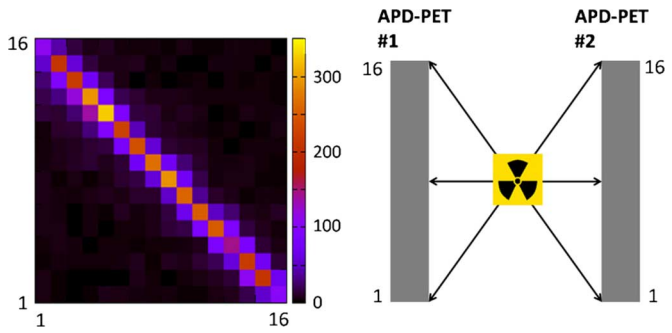

Fig. 10. (left) Coincidence diagram constructed between APD-based PET modules #1 and #2. (right) Schematic chart for the experimental setup, seen from the top view.

gamma-rays clearly exhibit a sharp trajectory in the matrix, thus indicating the correct functioning of the example system.

C. Image Reconstruction

The spatial resolution at the four positions (along the x-axis in the radial direction) of the center, and 0.5, 1.0 and 5.0 mm respectively, were measured using an $^{22}\mathrm{Na}$ point source as described above (Fig. 9). Coincidence events were taken at eleven positions by changing the roll angle (θ) at 18 degree intervals from 0 to 180 degrees. At each step >50,000 coincidence events were amassed with typical count rates of less than 100 cps.

Filtered Back Projection (FBP) was used to evaluate the spatial resolution of the preliminary test system. First the list mode data was transformed into a sinogram. The two crystal positions in each coincidence event, which define the Line-Of-Response (LOR), were then randomly determined according to the uniform distribution of the coincidence crystals and the FBP with a ramp filter without cutoff was then applied. The sinogram was sampled assuming the use of 20 detectors (18 degrees each) and thus 20 views. Fig. 11 provides example sinograms and the resultant reconstructed images obtained for the center and off-center (5.0 mm), respectively. The radial FWHM resolution was estimated at 0.9, 1.6, 1.4 and 1.3 mm respectively for the center, and 0.5, 1.0 and 5.0 mm off axis.

D. Comparison With Simulation

The prototype gantry detector configuration consisted of only two APD-based PET modules that were fixed on opposite sides of the gantry. Consequently, the experimental data could not be used to determine how the effect of varying depth of interaction affected the position resolution for source locations away from the central axis $(\mathrm{x} > 5\ \mathrm{mm})$. Monte Carlo simulated data was therefore used to estimate the resolution performance at any radial and tangential distance from the center. More than 50,000 pairs of 511 keV back-to-back gamma-rays were generated from the source in a random direction. For simplicity, we assumed a ring of LYSO blocks, the inner diameter of which was 150 mm ϕ, with each block consisting of a 16 × 16 array of $13 \times 13 \times 10\ \mathrm{mm}^3$ LYSO pixels, namely, a *fully-designed* gantry of the experimental setup shown in Fig. 9. Only the pixel IDs, at which 511 keV gamma-rays are photo-absorbed, were recorded because in actual experiments, it is virtually impossible to determine the exact positions of gamma-ray absorption

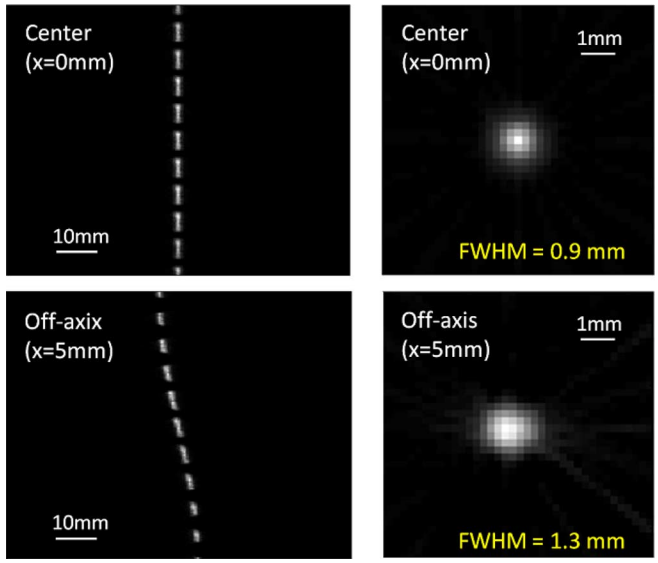

Fig. 11. Sinogram and FBP reconstructed image measured with a point source placed at the center (upper) and off-axis position of $\mathrm{x} = 5\ \mathrm{mm}$ (lower).

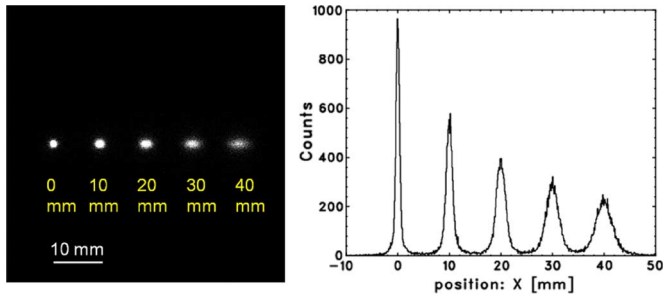

Fig. 12. (left) Simulated images of $^{22}\mathrm{Na}$ point source for a full-gantry of APD-based PET scanner described in the text. (right) Radial profile of the image projected on to x-axis.

within each LYSO pixel. Using this simulated data base, the image was reconstructed as for experimental data. The validity of the simulation could also be tested by direct comparison with the experimental data taken with source locations away from the central axis, as presented in the previous section. We simulated a point source positioned in the center and off-axis, from 0.5 mm to 40 mm. Fig. 12 provides the resultant simulated images from various source positions and its projection onto the radial axis. Note that the FWHM resolutions expected from the simulation correlated well with the experimental data, at 0.9 and 1.4 mm at the center and off-axis (5 mm), respectively. The simulated predicted Point Spread Functions (PSFs) would be non circular for far off-axis positions. The radial FWHM resolution degraded to 3.6 mm at $\mathrm{x} = 40\ \mathrm{mm}$. A comparison of the radial FWHM resolution with the experimental results and simulation is provided in Fig. 13 (filled circles and long/short dashed lines).

E. Example Study of the DOI Configuration

Similar to typically available commercial PET scanners our experimental preliminary gantry was not sensitive to the DOI of the photons in the scintillators, which resulted in the significant parallax error revealed in Fig. 13. Several ideas/designs for providing DOI information over the total detector volume free of

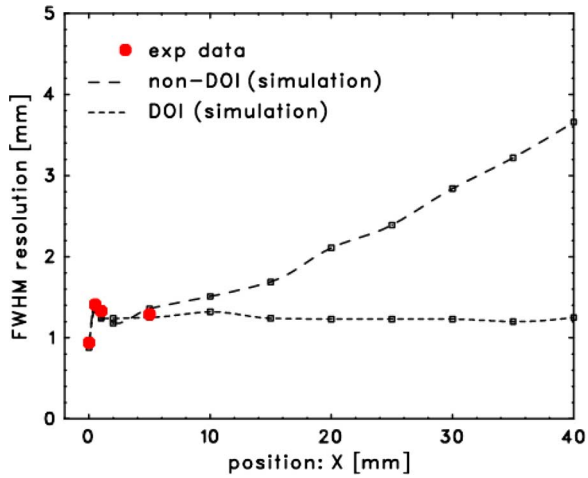

Fig. 13. The FWHM resolution for the APD-based PET detectors as a function of radial distance from the center. *Filled circle*: measurement data using two faced modules, *long dashed line*: simulation of the non-DOI configuration, *short dashed line*: simulation of the DOI configuration assuming a full-gantry.

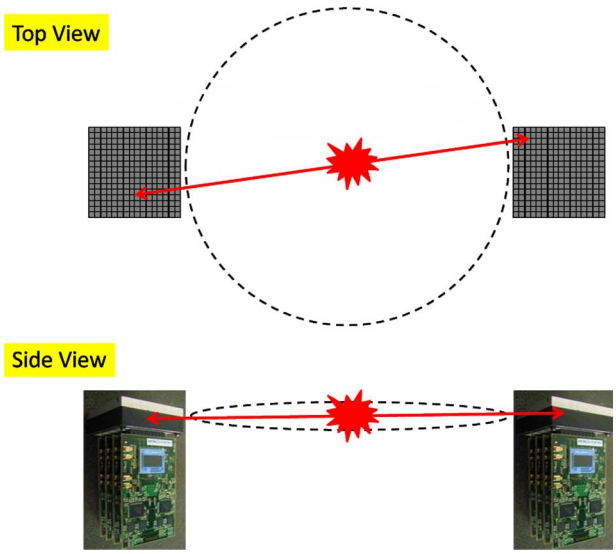

Fig. 14. Schematic geometry of toy model for the DOI detectors using APD-based modules. (upper) top view (lower) side view. In contrast to actual experimental setup shown in Fig. 12, simulation was performed when the modules are placed perpendicular to the ring gantry.

parallax errors have been proposed (e.g., [16]–[20]). As a subsequent step, we are planning to develop a DOI detector as an application of the APD-PET module described here. This motivated us to verify how the image resolution would be improved if the DOI could be measured correctly. In this section, a simple case featuring the APD-based PET modules positioned perpendicularly to the ring gantry, i.e., as the axially oriented arrays shown in Fig. 14, was considered. Moreover, simulated images at various source locations, corresponding to the non-DOI case in Fig. 12, are provided in Fig. 15. Even with this simple configuration, the resolution remained at the almost constant value of $\mathrm{FWHM} = 1.2\ \mathrm{mm}$ in both radial and tangential directions up to $\mathrm{x} = 40\ \mathrm{mm}$, suggesting the interesting potential for future DOI detectors to utilize compact APD-based PET modules.

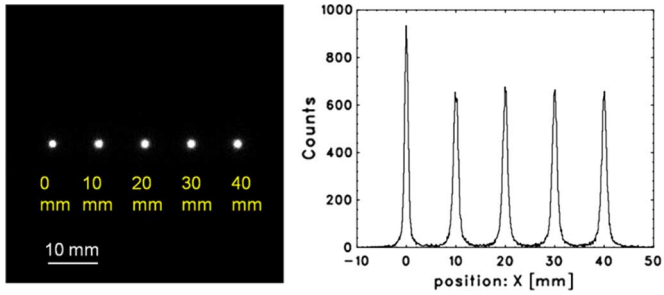

Fig. 15. (left) Simulated images of $^{22}\mathrm{Na}$ point source for a full-gantry of *DOI-sensitive* APD-based PET scanner described in the text. See Fig. 14 for schematic view of assumed geometry. (right) Radial profile of the image projected on to x-axis.

V. Conclusion

In this work, a prototype system for a high-resolution APD-based PET scanner, having achieved sub-millimeter spatial resolution was proposed. A detector module consisting of a large area reverse-type APD array, LYSO scintillator matrix and FECs all implemented in a small module $30 \times 30 \times 80\ \mathrm{mm}^3$ in size was successfully developed. At this stage, a pair of modules and a coincidence circuit were assembled into an experimental prototype gantry for use in evaluating its spatial resolution in point source measurements. The radial spatial resolution of the APD-based PET detector was estimated at 0.9 mm (center), 1.3 mm (5 mm off-center) and 3.6 mm (40 mm off-center) from a FBP reconstructed image. A very simple simulation suggested that the resolution uniformity could be improved considerably by using DOI information, resulting in a uniform $\sim$1.2 mm FWHM resolution over the field-of-view. These conclusions have encouraged us to develop future APD-based modules for use in extremely fine resolution PET scanners.

Acknowledgment

The authors thank the anonymous referees for their helpful comments to improve the manuscript. The authors would also like to thank Prof. N. Kawai and his students at the Tokyo Institute of Technology for their support and help in the experiments. Thanks also to Prof. H. Murayama from the NIRS for his helpful comments and encouragement.

References

[1] P. P. Webb, R. J. McIntyre, and J. Conradi, "Properties of avalanche photodiodes," *RCA Rev.*, vol. 35, pp. 234–278, 1974.

[2] R. Grazioso, N. Zhang, J. Corbeil, M. Schmand, R. Ladebeck, M. Vester, G. Schnur, W. Renz, and H. Fischer, "APD-based PET detector for simultaneous PET/MR imaging," *Nucl. Instrum. Methods Phys. Res. A*, vol. A569, pp. 301–305, Dec. 2006.

[3] B. J. Pichler, M. S. Judenhofer, C. Catana, J. H. Walton, M. Kneilling, R. E. Nutt, S. B. Siegel, C. D. Claussen, and S. R. Cherry, "Performance test of an LSO-APD detector in a 7-T MRI scanner for simultaneous PET/MRI," *J. Nucl. Med.*, vol. 47, no. 4, pp. 639–647, 2006.

[4] M. Bergeron *et al.*, "Performance evaluation of the LabPET APD-based digital PET scanner," *IEEE Trans. Nucl. Sci.*, vol. 56, no. 1, pp. 10–16, Feb. 2009.

[5] D. P. McElroy, W. Pimpl, B. J. Pichler, M. Rafecas, T. Schüler, and S. I. Ziegler, "Characterization and readout of MADPET-II detector modules: Validation of a unique design concept for high resolution small animal PET," *IEEE Trans. Nucl. Sci.*, vol. 52, no. 1, pp. 199–204, Feb. 2005.

[6] C. Woody *et al.*, "RatCAP: A small, head-mounted PET tomography for Imaging the brain of an awake RAT," *Nucl. Instrum. Methods Phys. Res. A*, vol. A527, pp. 166–170, Jul. 2004.

[7] C. Woody *et al.*, "Initial studies using the RatCAP conscious animal PET tomograph," *Nucl. Instrum. Methods Phys. Res. A*, vol. A571, pp. 14–17, Feb. 2007.

[8] C. Woody *et al.*, "Preliminary studies of a simultaneous PET/MRI scanner based on the RatCAP small animal tomography," *Nucl. Instrum. Methods Phys. Res. A*, vol. A571, pp. 102–105, Feb. 2007.

[9] R. Lecomte, "Technology challenges in small animal PET imaging," *Nucl. Instrum. Methods Phys. Res. A*, vol. A527, pp. 157–165, Jul. 2004.

[10] S.-J. Park *et al.*, "A prototype of very high-resolution small animal PET scanner using silicon pad detectors," *Nucl. Instrum. Methods Phys. Res. A*, vol. A570, pp. 543–555, Jan. 2007.

[11] G. Llosá *et al.*, "Energy, timing and position resolution studies with 16-pixel silicon photomultiplier matrices for small animal PET," *IEEE Trans. Nucl. Sci.*, vol. 56, no. 5, pp. 2586–2593, Oct. 2009.

[12] T. Ikagawa *et al.*, "Performance of large-area avalanche photodiodes for low-energy X-rays and gamma-rays scintillation detection," *Nucl. Instrum. Methods Phys. Res. A*, vol. A515, pp. 671–679, Dec. 2003.

[13] J. Kataoka, T. Saito, Y. Kuramoto, T. Ikagawa, Y. Yatsu, J. Kotoku, M. Arimoto, N. Kawai, Y. Ishikawa, and N. Kawabata, "Recent progress of avalanche photodiodes in high-resolution X-rays and gamma-rays detection," *Nucl. Instrum. Methods Phys. Res. A*, vol. A541, pp. 398–404, Apr. 2005.

[14] J. Kataoka *et al.*, "Development of large-area, reverse-type APD -arrays for high-resolution medical imaging," *Nucl. Instrum. Methods Phys. Res. A*, vol. A604, pp. 323–326, Jun. 2009.

[15] M. Koizumi *et al.*, "Development of a low-noise analog front-end ASIC for APD-PET detectors," *Nucl. Instrum. Methods Phys. Res. A*, vol. A604, pp. 327–330, Jun. 2009.

[16] A. Braem *et al.*, "Novel design of a parallax free Compton enhanced PET scanner," *Nucl. Instrum. Methods Phys. Res. A*, vol. A525, pp. 268–274, Jun. 2004.

[17] T. Yamaya, N. Hagiwara, T. Obi, T. Tsuda, K. Kitamura, T. Hasegawa, H. Haneishi, N. Inadama, E. Yoshida, and H. Murayama, "Preliminary resolution performance of the prototype system for a 4-layer DOI-PET scanner; jPET-D4," *IEEE Trans. Nucl. Sci.*, vol. 53, no. 3, pp. 1123–1128, Jun. 2006.

[18] A. A. R. Fremout, R. Chen, P. Bruyndonckx, and S. P. K. Tavernier, "Spatial resolution and depth-of-interaction studies with a PET detector module composed of LSO and APD array," *IEEE Trans. Nucl. Sci.*, vol. 49, no. 1, pp. 131–138, Feb. 2002.

[19] J. S. Huber, W. W. Moses, S. E. Derenzo, M. H. Ho, M. S. Andreaco, M. J. Paulus, and R. Nutt, "Characterization of a 64 channel PET detector using photodiodes for crystal identification," *IEEE Trans. Nucl. Sci.*, vol. 44, no. 3, pp. 1197–1201, Jun. 1997.

[20] Y. Shao, R. W. Silverman, R. Farrell, L. Cirignano, R. Grazioso, K. S. Shah, G. Vissel, M. Clajus, T. O. Tumer, and S. R. Cherry, "Design studies of a high resolution PET detector using APD arrays," *IEEE Trans. Nucl. Sci.*, vol. 47, no. 3, pp. 1051–1057, Jun. 2000.